🔓 **Open Access**

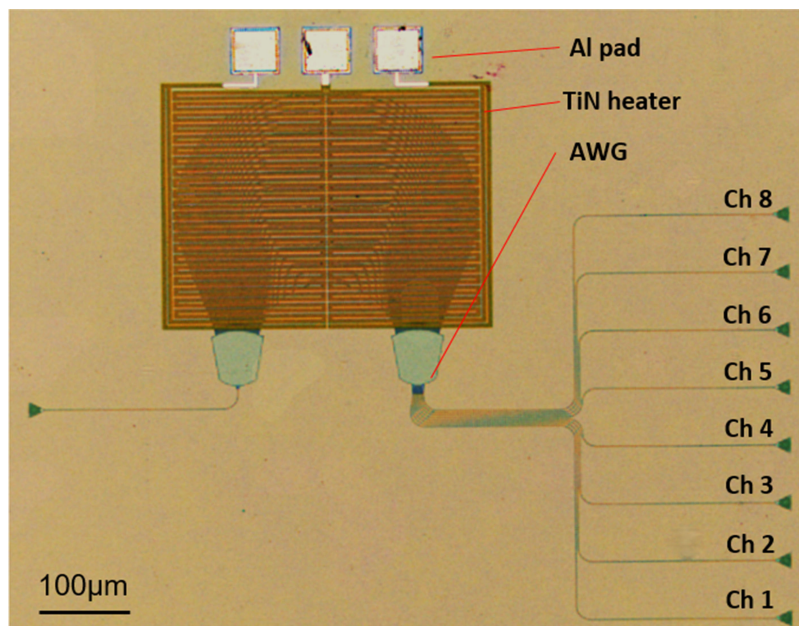# Thermo-Optic Tunable Silicon Arrayed Waveguide Grating at 2-$\mu$m Wavelength Band

**Yingjie Liu**
**Zhiyu Li**
**Di Li**
**Yong Yao**
**Jiangbing Du,** *Member, IEEE*
**Zuyuan He,** *Senior Member, IEEE*
**Ke Xu,** *Member, IEEE*

# Thermo-Optic Tunable Silicon Arrayed Waveguide Grating at 2-$\mu$m Wavelength Band

**Yingjie Liu,**[1] **Zhiyu Li,**[1] **Di Li,**[1] **Yong Yao** ⓘ**,**[1]
**Jiangbing Du** ⓘ**,**[2] ***Member, IEEE,***
**Zuyuan He** ⓘ**,**[2] ***Senior Member, IEEE,* and Ke Xu** ⓘ**,**[1] ***Member, IEEE***

[1]Department Electronic and Information Engineering, Harbin Institute of Technology
(Shenzhen), Shenzhen 518055, China
[2]State Key Laboratory of Advanced Optical Communication Systems and Networks,
Shanghai Jiao Tong University, Shanghai 200240, China

**Abstract:** The transparent window in optical fiber at 2-$\mu$m waveband enables a huge potential for fiber optical communications. Intensive efforts have been devoted to pursuit of photonic devices in this new band. The arrayed waveguide grating (AWG) is one of the key components for various functionalities like wavelength multiplexer, optical filter, spectrometer and so forth. However, the integrated and wavelength tunable AWG has not been realized in the 2-$\mu$m wavelength range yet. Here, we demonstrate an 8-channel thermo-optic tunable AWG at 2 $\mu$m via silicon photonic multi-project wafer shuttle run. The device is fully compatible with standard foundry fabrication process without customization. The TiN heater is designed for uniform waveguide heating and wavelength detuning. Experiments show that the fabricated AWG has a dense channel spacing of 1.6 nm and a minimum insertion loss of 6.1 dB. The wavelength tuning efficiency is measured to be 6.4 nm/W.

**Index Terms:** Integrated optics, arrayed waveguide grating (AWG), thermo-optic (TO) effect.

## 1. Introduction

Infrared lasers at wavelengths around 2-$\mu$m have proven applications in sensing [1]–[4], surgery [5], light detection and ranging system [6] and so forth. Recently, the 2-$\mu$m spectral range has opened a new avenue for optical communication applications. Though transmission experiments have been only demonstrated for limited distance, solid evidences have been observed for the great potential for optical interconnects [7], [8]. The communication window shifts to this waveband due to the ultra-low loss of optical fibers, the maturity of narrow linewidth lasers, thulium doped fiber amplifier with 30 THz gain bandwidth [9]–[11], high-speed photodiode [12]–[14], and modulator [15], [16]. The hollow core photonic bandgap fiber (HCPBF) is predicted to have a low latency [17] and an attenuation of only 0.1 dB/km at 2-$\mu$m wavelengths [18], which allow for a promising solution

for datacenter scenario [19], [20]. Driven by the increasing demand for integrated components with low cost and high performance in the new waveband, rapid progress has been made in various devices such as grating couplers [21], waveguide detectors [22], filters [23], mode multiplexers [24], power splitters [25] and etc. These devices are realized by silicon photonics which offer the advantages of large fabrication volume and potential low cost. It is also interesting to note that, long wavelength operation of the silicon photonic device has much smaller signal penalties due to nonlinear absorptions.

As a fundamental building block for photonic integrated circuits, arrayed waveguide gratings (AWG) play important roles in on-chip spectroscopy [26] and wavelength division multiplexing (WDM) [19], [27]. It has distinct advantages over other alternative device structures for multi-channel narrow band filtering. Due to its unique applications, AWG have been widely demonstrated in C-band on various integration platforms [28]–[33]. An InP-based AWG operated at 2-$\mu$m is first demonstrated for WDM transmission to increase the data capacity [26]. More recently, silicon photonic AWG has been reported on silicon-on-insulator (SOI) substrate near 2-$\mu$m wavelength. But a thick silicon device layer of 500 nm is needed to accommodate long-wavelength optical wave, and the operation wavelengths of the AWG cannot be tuned [34].

In this work, we demonstrate a wavelength tunable AWG which is designed following the standard design rules for silicon photonic foundry fabrication. The devices are fabricated on a standard SOI wafer via a multi-project wafer (MPW) shuttle run. The fabrication shares the same process that is optimized for C-band devices, and no customized process is needed for the proposed 2-$\mu$m AWG. The wavelength multiplexer is also integrated with metal heaters to enable the detuning of the operation wavelength. The co-integration with C-band devices allows for multi-waveband on-chip applications like ultra-broadband spectrometer for chemical sensing and ultra-large capacity data communications.

## 2. Design and Fabrication

The 2-$\mu$m tunable AWG is designed on SOI wafer with 220 nm top silicon and 2 $\mu$m buried oxide (BOX). According to the working principle of the Rowland circle, the AWG satisfies the following grating equation:

$$n_{s,eff}d_a \sin\theta_i + n_{s,eff}d_a \sin\theta_o + n_{c,eff}\Delta L = m\lambda \qquad (1)$$

where $n_{s,eff}$ and $n_{c,eff}$ are the effective indice of the slab region and arrayed waveguide, respectively. $\theta_i$ and $\theta_o$ are the off-normal angles between the central input/output waveguides and the Rowland circle, $\Delta L$ is the length difference of arrayed waveguides, $m$ is the diffraction order ($m = n_{c,eff}\Delta L/\lambda$), and $\lambda$ is the operation wavelength. Eqn (1) indicates that the path difference$\Delta L$ of the AWG increases for long wavelength operation due to increased wavelength $\lambda$ and reduced effective refractive indice $n_{s,eff}$ and $n_{c,eff}$. As a result, the 2-$\mu$m AWG is larger in footprint compared to 1550-nm waveband, and the transmission loss is also increased. Therefore, it is more challenging to design a high-performance long-waveband AWG device.

For a design target of 1.6 nm ($\sim$120 GHz at 2-$\mu$m) channel spacing, 60 arrayed waveguides are designed with a waveguide length difference $\Delta L$ of 18.7 $\mu$m according to Eqn. (1). The diameter of the Rowland circle is chosen to be 120 $\mu$m. The top-view and cross section schematic diagram of the designed AWG is shown in Fig. 1(a) and (b). The waveguide core is 600 nm-wide with 220 nm full etching depth to ensure the single mode operation and low scattering loss from sidewall roughness at 2-$\mu$m band. The minimum bending radius of the waveguide is defined as 20 $\mu$m to minimize the radiation loss. Fig. 1(c) show the simulated top-view and cross-section optical field distribution of the strip silicon waveguide with 20-$\mu$m radius by 3D FDTD method. The calculated radiation loss is only $\sim$0.012 dB/90°bend. The effective refractive index of silicon waveguide with different widths is shown in Fig. 1(d). The linear adiabatic taper is designed to reduce the coupling losses from the Rowland circle to the array waveguide and the input/output waveguide. To further alleviate the impact from sidewall roughness, a 70-nm shallow-etch process is chosen in the taper region to further reduce the device loss which is shown on the fabricated AWG in Fig. 5(b) and (c).
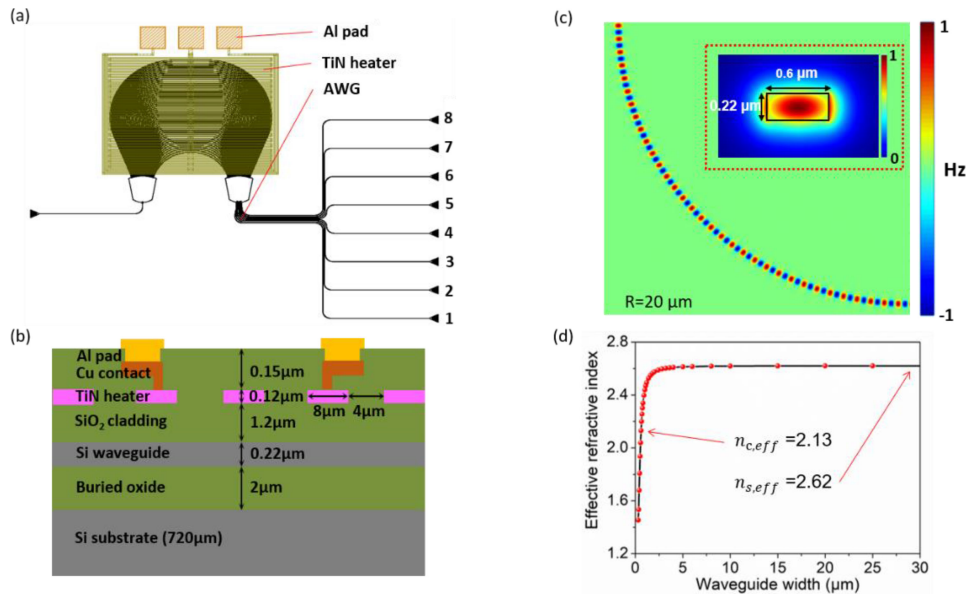
Fig. 1. (a) The layout of the designed 2-$\mu$m wavelength tunable AWG. (b) The cross-sectional schematic view of the AWG structure. (c) The calculated top-view and cross-section optical field distribution of the strip waveguide with 20-$\mu$m radius for TE mode at 2-$\mu$m. (d) The calculated effective refractive index for TE$_0$ mode under different silicon waveguide widths.

The TE-polarization grating couplers are designed with 10-degree tilt in both the input and output ports to reduce the back reflection. The grating coupler has 220 nm etching depth and can operate at 2-$\mu$m waveband with simulated coupling efficiency of $-4.5$ dB. The period of the grating coupler is 950 nm with a filling factor of 0.23. The output grating couplers are arranged in an array with 127 $\mu$m pitch which can be interfaced with a commercial fiber array. The footprint of the whole device layout is $\sim$1.6 mm$\times$1.3 mm.

We build the AWG model in Lumerical Mode Solutions for waveguide design. Since the arrayed waveguide region is too large in area, the simulations consume huge amount of computational memory and time. Here we use the time delay to emulate the waveguide array with a certain length difference in the simulation model. The time delay can be expressed by the following equation:

$$\Delta t = \Delta L / v_g \qquad (2)$$

where $v_g$ is the group velocity ($v_g = c/n_g$), $c$ is light velocity in vacuum, $n_g$ is the group refractive index. In this way, we can simulate and plot the optical field profile of the output free propagation region in Fig. 2(a). The simulated transmission spectrum of the AWG is also obtained as shown in Fig. 2(b). It can be seen that the channel spacing is 1.6 nm and the insertion loss is $\sim$3.5 dB. Since the waveguide array transmission is not performed in the model, the simulated loss is a bit underestimated.

Al pads and TiN heaters are designed for wavelength tuning via thermo-optic (TO) effect. As shown in Fig. 1(b), high-resistivity TiN heaters with 0.12 $\mu$m thickness are designed on top of the arrayed waveguide to tune the center wavelength of the AWG passbands. There is 1.2-$\mu$m-thick SiO$_2$ cladding sandwiched between the metal and waveguides to avoid high loss. The top-view layout of the designed TiN heater is shown in Fig. 3(a). It can be seen that the heater strip has a width of 8 $\mu$m, and the array of heaters with a spacing of 4 $\mu$m is densely patterned. The arrayed heaters are designed in parallel and symmetrically arranged with respect to the central axis of the waveguide array, which allows for efficient and uniform waveguide heating. As shown in Fig. 3(b), the resistance of the designed heater is calculated to be $R = \frac{1}{\frac{1}{R1} + \frac{1}{R2}} + R3 + R4 = 3630 \ \Omega$. For the finalized AWG design, the main parameters of the device structure are summarized in Table 1.
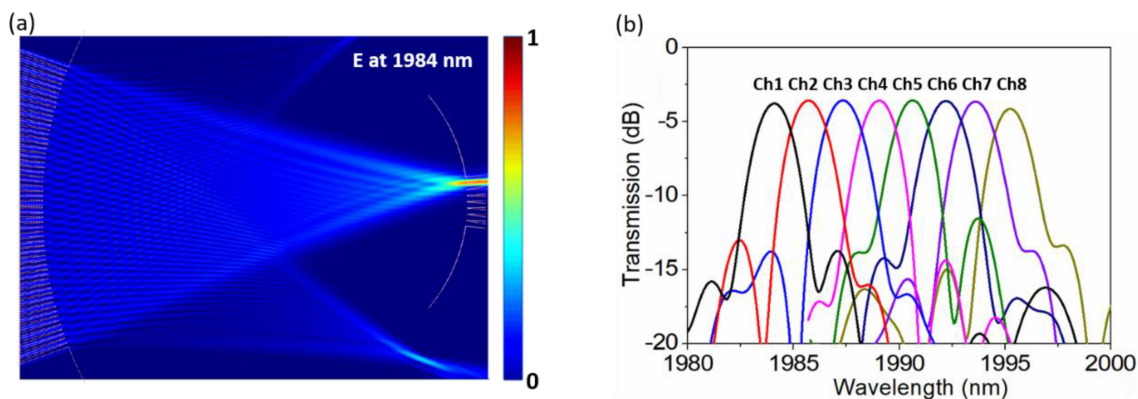
Fig. 2. (a) The simulated optical field distribution (E) of the output free propagation region. (b) The simulated transmission spectrum of the designed AWG.
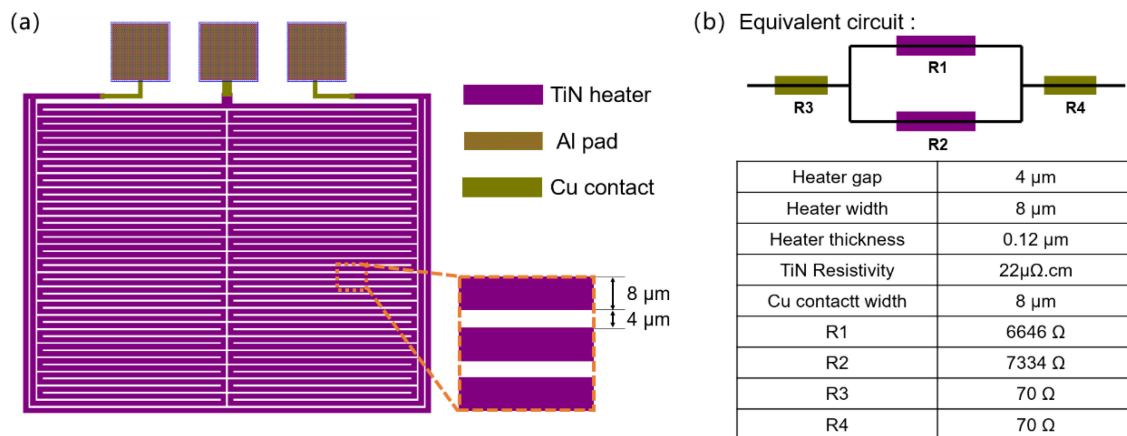


Fig. 3. (a) The top-view layout of TiN heater. (b)The equivalent circuit and the related parameters.

TABLE 1

Designed Parameters of the 2-$\mu$m TO AWG

| Parameter | Symbol | Value | Parameter | Symbol | Value |
|---|---|---|---|---|---|
| Center wavelength | $\lambda_0$ | 2000 nm | Diameter of Rowland circle | $D$ | 120 μm |
| Channel spacing | $\Delta\lambda$ | 1.6 nm | Diffraction order | $m$ | 25 |
| Minimum bending radius | $r_m$ | 20 μm | Spacing of arrayed waveguide | $d_a$ | 1.5 μm |
| Path diffrence | $\Delta L$ | 18.7 μm | Heater width | $d_w$ | 8 μm |
| Number of output channels | $N_o$ | 8 | Heater spacing | $d_s$ | 4 μm |
| Number of arrayed waveguides | $N_a$ | 60 | Designed resistance | $R$ | 3630 Ω |

To better understand the TO tuning effect of the proposed AWG, here we theoretically calculate the wavelength shift of the device. From Eqn. (1), we can see that the refractive index of the arrayed waveguide varies with the temperature, and the wavelength is shifted accordingly. The corresponding wavelength shift $\Delta\lambda$ as a function of the index change can be expressed as:

$$\Delta\lambda = \Delta n_c \lambda / n_{c,eff} \qquad (3)$$

where $\Delta n_c$ is the waveguide effective refractive index change due to temperature variation.
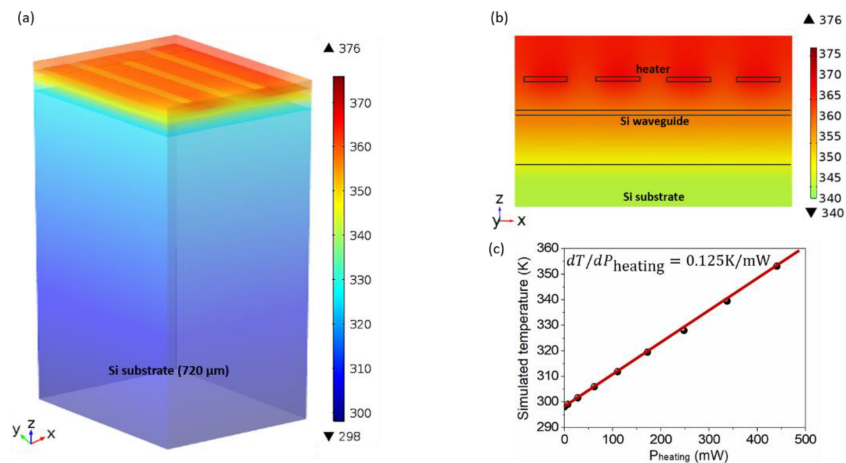
Fig. 4. (a) The simulated 3D temperature distribution of the AWG heat-transfer model. (b) The partial cross-section temperature distribution of the model. (c) Calculated temperature of the silicon waveguide under different powers on TiN heater.

Then, we built a 3D heat transfer model based on the design parameters as shown in Table 1 to calculate the temperature distribution of the AWG structure via COMSOL Multiphysics commercial software. The calculation is performed by a MEAS Module of the electro-thermal structure which is modeled by Poisson equation and heater transfer equation. The electric conductivity and thermal conductivity of TiN materials is defined as 454.6 S m$^{-1}$ and 29.3 W m$^{-1}$K$^{-1}$, respectively. The thermal conductivity is set to 80 W m$^{-1}$K$^{-1}$ for silicon and 1.4 W m$^{-1}$K$^{-1}$ for silica, respectively. The heat convection coefficient of air is set to $\sim$ 5 W m$^{-2}$K$^{-1}$, and the room temperature (RT) is 298.15 K in this model. Fig. 4(a) shows the simulated temperature distribution of the 3D device model when the applied electrical voltage is $V_{heating}$ = 40 V (440 mW). The power density is $\sim$ 7.3 $\times$ 10$^{-3}$ mW $\mu$m $^{-3}$. It can be clearly seen from the temperature distribution that the TiN heater has the highest temperature, and the temperature drops gradually towards room temperature from the top to silicon substrate. Fig. 4(b) shows the cross-sectional temperature distribution of the AWG model, which confirms that the silicon waveguide layer is almost uniformly heated up with temperature increased by $\sim$ 55 K. Fig. 4(c) is the calculated temperature of the silicon waveguide under different powers. The temperature almost changes linearly as a function of the heating power. The linearly fitted slope is $dT/dP_{heating} = 0.125\ K/mW$. Such a uniformity for waveguide heating is important for stable and linear wavelength detuning of the wavelengths.

Then, the devices are fabricated by the silicon photonic MPW shuttle run where the waveguide is defined by 193 nm UV lithography and then transferred to silicon layer via dry etching process. Fig. 5(a) shows the top-view microscope image of the fabricated 1×8 tunable AWG. The device is well fabricated as we designed and is co-integrated with other O-band and C-band devices on the same chip. Fig. 5(b)-(c) are the zoom-in images of the free propagation region between the array waveguides and output waveguides. The green area is the 70 nm etched silicon slab which ensures low scattering loss from the sidewall roughness. The minimum gap size of the linear taper is 0.2 $\mu$m, which is the allowed minimum feature size for low coupling loss of the free propagation region to the array/output waveguides. Fig. 5(d) is the close-up microscope image of the fabricated focus grating coupler.

# 3. Results and Discussions

To characterize the 2-$\mu$m AWG, we setup the system using a narrow line width 2-$\mu$m band tunable laser (OETLS-300-2000), a fiber-chip coupling stage, DC probes, an InGaAs optical power meter (S148C), and a Keithley 2450 SourceMeter. The light is coupled into/out the silicon waveguides
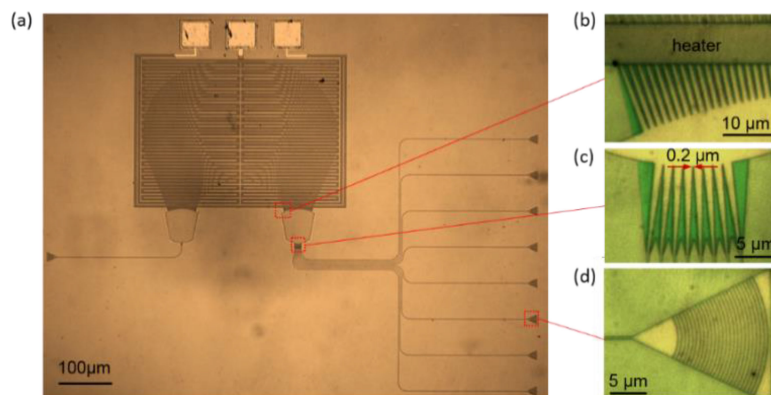
Fig. 5. (a) The top-view microscope image of the fabricated tunable AWG. (b) The zoom-in image of the free propagation region to the array waveguide. (c) The zoom-in image of the free propagation region to the output waveguide. (d) The close-up image of the focus grating coupler.
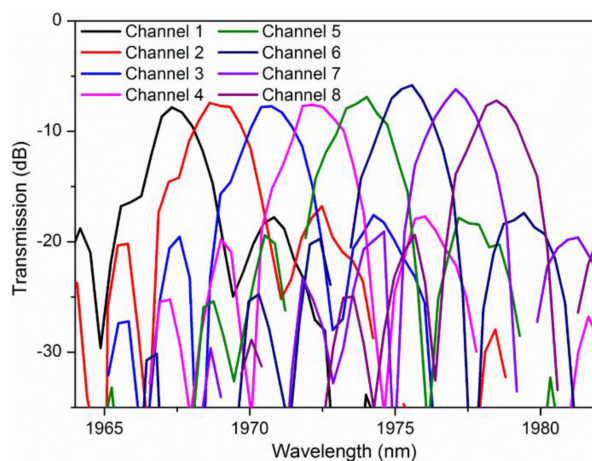


Fig. 6. The measured transmission spectra of the fabricated 8-channel AWG at 2-$\mu$m waveband.

via a pair of grating couplers. The coupling loss per facet is measured to be approximately 7 dB at 1980 nm. The measured transmission spectra of the 8 output channels are normalized and plotted in Fig. 6. It can be observed that the center wavelength has a 27 nm offset from the designed center wavelength of 2000 nm due to the phase error. The channel spacing is measured to be ~1.6 nm, which is well consistent with the design target. The measured insertion loss of different channels ranges from −6.1 dB to −7.8 dB. The loss difference is due to the different waveguide length and curvature radius for each channel.

The loss mechanisms of the AWG mainly come from the waveguide propagation loss due to the silicon waveguide sidewall roughness in fabrication process. While the intrinsic absorption loss in silicon waveguide and $SiO_2$ layer is negligible at 2000 nm wavelength, the narrow width of the arrayed waveguide magnifies the impact from sidewall roughness which results in significant scattering loss and crosstalk [35], [36]. Though increasing the waveguide width can reduce the loss from sidewall roughness, it increases the radiation loss in the bending area. Considering the trade-off between radiation losses and sidewall scattering losses, waveguides with non-uniform width can be applied to further optimize the device losses. The narrow waveguide can be used in bending region, and wide waveguide can be used for straight waveguide region. The transitioned can be realized by an adiabatic taper. In addition, the phase error is also caused by the non-uniform change of the silicon waveguide effective refractive index in propagation process due to rough
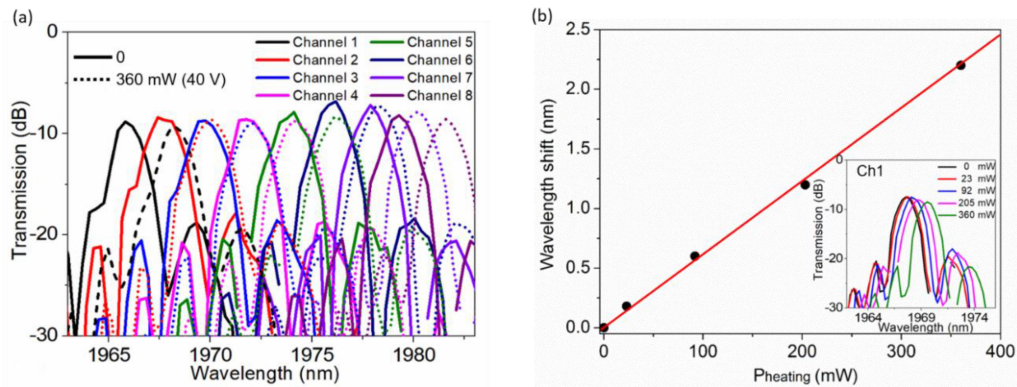
Fig. 7. (a) The transmission spectra of Ch1-8 with 0 mW and 360 mW applied electrical power. (b) The wavelength shift of Ch 1 under different applied electrical power $P_{heating}$, inset: the transmission spectra of Ch 1 with different power.

sidewalls and tilted waveguide sidewalls. the phase error makes it challenging to precisely control the center wavelength of the AWG. Thus, it is highly desirable to compensate the wavelength shift using TO phase shifter.

Then, we characterize the TO performance of the tunable AWG. The transmission spectra of the 8 output channels are measured under different electrical power applied to the TiN heater via a Source Meter. Fig. 7(a) shows the transmission spectra of channel 1-8 with different electrical power ($P_{heating}$). It can be observed that the spectrum is red-shifted by ∼2.3 nm with $P_{heating}$ = 360 mW, which is beyond a channel spacing of 1.6 nm. This indicates that we can accurately control the channel wavelength of the AWG by fine tuning of the heater and handle arbitrary wavelength within the AWG pass band. As shown in Fig. 7(b), the wavelength is shifted almost linearly with different electrical power ($P_{heating}$) which implies a good linearity of the TO tuning. The experiment results show that the channel tuning efficiency is 6.4 nm/W. We also extract the resistance of the heater from the experiment which is ∼4400 Ω. The difference between the calculated and measured resistance is mainly due to the additional contact resistance, such as layer-contact (Al/Cu/TiN) resistance, probe-electrode contact resistance in measurement. The tuning efficiency of the heater can be further improved by optimizing the layout of the heater array to reduce resistance such as using the parallel heater-structure layout and increasing heater-waveguide width.

## 4. Conclusion

In conclusion, we experimentally demonstrate an 8-channels wavelength tunable AWG on SOI platform at 2-$\mu$m waveband. The device is fabricated on a standard silicon photonic multi-project wafer and is fully compatible with the design rule for 1.55 $\mu$m components. The AWG is measured to have a dense channel spacing (120 GHz) and a minimum insertion loss of 6.1 dB. The operation wavelength of the AWG can be thermally tuned with an efficiency of 6.4 nm/W. The wavelength can be easily tuned across one channel spacing which allows the AWG to operate at arbitrary wavelength within its spectral band. The possibility of co-integration with C band components can potentially enable ultra-broadband photonic integrated circuits.

## References

[1] P. Werle, F. Slemr, K. Maurer, R. Kormann, R. Mucke, and B. Janker, "Near- and mid-infrared laser-optical sensors for gas analysis," *Opt. Lasers Eng.* vol. 37, no. 2, pp. 101–114, 2002.

[2] B. Mizaikoff, "Waveguide-enhanced mid-infrared chem/bio sensors," *Chem. Soc. Rev.* vol. 42, no. 22, pp. 8683–8699, 2013.

[3] K. Xu *et al.*, "Optical fiber humidity sensor based on water absorption peak near 2-$\mu$m waveband," *IEEE Photon. J.*, vol. 11, no. 2, pp. 1–8, Apr. 2019.

[4] L. Zhang and D. Dai, "Silicon subwavelength-grating microdisks for optical sensing," *IEEE Photon. Technol. Lett.*, vol. 31, no. 15, pp. 1209–1212, Aug. 2019.

[5] B. Chen, S. L. Thomsen, R. J. Thomas, J. Oliver, and A. J. Welch, "Histological and modeling study of skin thermal injury to 2.0 $\mu$m laser irradiation," *Lasers Surg. Med.*, vol. 40, no. 5, pp. 358–370, 2008.

[6] J. J. Ackert *et al.*, "High-speed detection at two micrometres with monolithic silicon photodiodes," *Nature Photon.*, vol. 9, no. 10, pp. 393–396, 2015.

[7] K. Xu, L. Sun, Y. Q. Xie, Q. Song, J. B. Du, and Z. He, "Transmission of IM/DD signals at 2 $\mu$m wavelength using PAM and CAP," *IEEE Photon. J.*, vol. 8, no. 5, pp. 1–7, Oct. 2016.

[8] K. Xu, Q. Wu, Y. Xie, M. Tang, S. Fu, and D. Liu, "High-speed single-wavelength modulation and transmission at 2 $\mu$m under bandwidth-constrained condition," *Opt. Express*, vol. 25, no. 4, pp. 4528–4534, 2017.

[9] Z. Li *et al.*, "Diode-pumped wideband thulium-doped fiber amplifiers for optical communications in the 1800–2050 nm window," *Opt. Express*, vol. 21, no. 22, pp. 26450–26455, 2013.

[10] Z. Li, A. M. Heidt, J. M. O. Daniel, Y. Jung, S. U. Alam, and D. J. Richardson, "Thulium-doped fiber amplifier for optical communications at 2 $\mu$m," *Opt. Express*, vol. 21, no. 8, pp. 9289–9297, 2013.

[11] A. M. Heidt, Z. Li, and D. J. Richardson, "High power diodeseeded fiber amplifiers at 2 $\mu$m–from architectures to applications," *IEEE J. Sel. Topics Quantum Electron.*, vol. 20, no. 5, pp. 525–536, Sep.-Oct. 2014.

[12] Y. Dong *et al.*, "Two-micron-wavelength germanium-tin photodiodes with low dark current and gigahertz bandwidth," *Opt. Express*, vol. 25, no. 14, pp. 15818–15827, 2017.

[13] Y. Peng, H. H. Chang, V. L. Mashanov, and G. Chang, "GeSn p-i-n waveguie photodetectors on silicon substrates," *Appl. Phys. Lett.*, vol. 105, no. 23, pp. 1109–1114, 2014.

[14] M. Muneeb *et al.*, "Silicon-on-insulator shortwave infrared wavelength meter with integrated photodiodes for on-chip laser monitoring," *Opt. Express*, vol. 22, no. 22, pp. 27300–27308, 2014.

[15] K. Xu, G. K. P. Lei, S. M. G. Lo, Z. Cheng, C. Shu, and H. K. Tsang, "Bit-rate-variable DPSK demodulation using silicon microring resonators with electro-optic wavelength tuning," *IEEE Photon. Technol. Lett.*, vol. 24, no. 14, pp. 1221–1223, Jul. 2012.

[16] X. Wu, C. Huang, K. Xu, C. Shu, and H. K. Tsang, "128-Gb/s line rate OFDM signal modulation using an integrated silicon microring modulator," *IEEE Photon. Technol. Lett.*, vol. 28, no. 19, pp. 2508–2561, Oct. 2016.

[17] Y. Chen *et al.*, "Multi-kilometer long, longitudinally uniform hollow core photonic bandgap fibers for broadband low latency data transmission," *J. Lightw. Technol.*, vol. 34, no. 1, pp. 104–113, Jan. 2016.

[18] M. U. Sadiq *et al.*, "40 Gb/s WDM transmission over 1.15-km HC-PBGF using an InP-based Mach-Zehnder modulator at 2 $\mu$m," *J. Lightw. Technol.*, vol. 34, no. 8, pp. 1706–1711, Apr. 2016.

[19] H. Zhang *et al.*, "100 Gbit/s WDM transmission at 2 $\mu$m: Transmission studies in both low-cost hollow core photonic bandgap fiber and solid core fiber," *Opt. Express*, vol. 23, no. 4, pp. 4946–4951, 2015.

[20] C. W. Chow, C. H. Yeh, S. M. G. Lo, C. Li, and H. K. Tsang, "Long-reach radio-over-fiber signal distribution using single-sideband signal generated by a silicon-modulator," *Opt. Express*, vol. 19, no. 12, pp. 11312–11317, 2011.

[21] J. Li *et al.*, "2-$\mu$m wavelength grating coupler, bent waveguide, and tunable microring on silicon photonic MPW," *IEEE Photon. Technol. Lett.*, vol. 30, no. 5, pp. 471–474, Mar. 2018.

[22] Y. Yin *et al.*, "High-speed and high-responsivity hybrid silicon/black-phosphorus waveguide photodetectors at 2 $\mu$m," *Laser Photon. Rev.*, vol. 13, no. 6, 2019, Art. no. 1900032.

[23] D. Liu, H. Wu, and D. Dai, "Silicon multimode waveguide grating filter at 2 $\mu$m," *J. Lightw. Technol.*, vol. 37, no. 10, pp. 2217–2222, May 2019.

[24] S. Zheng *et al.*, "Silicon-based four-mode division multiplexing for chip-scale optical data transmission in the 2 $\mu$m waveband," *Photon. Res.*, vol. 7, no. 9, pp. 1030–1035, 2019.

[25] H. Xie *et al.*, "Inversely designed 1×4 power splitter with arbitrary ratios at 2-$\mu$m spectral band," *IEEE Photon. J.*, vol. 10, no. 4, pp. 1–6, Aug. 2018.

[26] E. J. Stanton, M. J. R. Heck, J. Bovington, A. Spott, and J. E. Bowers, "Multi-octave spectral beam combiner on ultra-broadband photonic integrated circuit platform," *Opt. Express*, vol. 23, no. 9, pp. 11272–11283, 2015.

[27] H. Zhang *et al.*, "Dense WDM transmission at 2 $\mu$m enabled by an arrayed waveguide grating," *Opt. Lett.*, vol. 40, no. 14, pp. 3308–3311, 2015.

[28] J. Dieckröger, R. März, P. C. Clemens, G. Heise, and H. W. Schneider, "Thermooptically tunable optical phased array in SiO2-Si," *IEEE Photon. Technol. Lett.*, vol. 11, no. 2, pp. 248–250, Feb. 1999.

[29] H. Bissessur, F. Gaborit, B. Martin, G. Ripoche, and P. Pagnod-Rossiaux, "Tunable phased-array wavelength demultiplexer on InP," *Electron. Lett.*, vol. 31, no. 1, pp. 32–33, 1995.

[30] M. Kohtoku, H. Sanjoh, Y. Kadota, and Y. Yoshikuni, "Packaged polarization-insensitive WDM monitor with low loss (7.3 dB) and wide tuning range (4.5 nm)," *IEEE Photon. Technol. Lett.*, vol. 10, no. 11, pp. 1614–1616, Nov. 1998.

[31] H. Zhang *et al.*, "Thermo-optically tunable arrayed-waveguide grating made of polymer/Si," *Optoelectron. Lett.*, vol. 2, no. 4, pp. 243–245, 2006.

[32] S. Toyoda *et al.*, "Polarization-independent low-crosstalk polymeric AWG-based tunable filter operating around 1.55 $\mu$m," *IEEE Photon. Technol. Lett.*, vol. 11, no. 9, pp. 1141–1143, Sep. 1999.

[33] Y. Yang *et al.*, "Thermo-optically tunable silicon AWG with above 600 GHz channel tunability," *IEEE Photon. Technol. Lett.*, vol. 27, no. 22, pp. 2351–2354, Nov. 2015.

[34] E. J. Stanton, N. Volet, and J. E. Bowers, "Silicon arrayed waveguide gratings at 2.0-$\mu$m wavelength characterized with an on-chip resonator," *Opt. Lett.*, vol. 43, no. 5, pp. 1135–1138, 2018.

[35] P. Dong *et al.*, "Low loss shallow-ridge silicon waveguides," *Opt. Express* vol. 18, no. 14, pp. 14474–14479, 2010.

[36] F. Grillot, L. Vivien, S. Laval, D. Pascal, and E. Cassan, "Size influence on the propagation loss induced by sidewall roughness in ultrasmall SOI waveguides," *IEEE Photon. Technol. Lett.*, vol. 16, no. 7, pp. 1661–1663, Jul. 2004.